RSC Advances

ROYAL SOCIETY OF CHEMISTRY

www.rsc.org/advances

Ellipsoid-like $Li_4Ti_5O_{12}$-TiO_2 composite constructed by nanocrystals for lithium ion batteries

Wenjun Zhu, Hui Yang and Xingzhong Guo *

School of Materials Science and Engineering, Zhejiang University, 38 Zheda Road, Xihu District, Hangzhou 310027, China.

Porous ellipsoid-like $Li_4Ti_5O_{12}$-TiO_2 composite with a unique micro/nano structure has been successfully fabricated via a facile sol-gel route followed by calcination. The porous ellipsoid-like particles with micro/nano structure are formed through phase-separation induced by poly(ethylene oxide) (PEO), which are constructed by numerous nanocrystals with sizes of about 50–100 nm and consisted of lithium titanate, anatase and rutile. The resultant $Li_4Ti_5O_{12}$-TiO_2 composite shows a superior rate capability and cycling stability in comparison with pure $Li_4Ti_5O_{12}$, which delivers a reversible capacity over 92 mAh g^{-1} at 10 C after 100 cycles as well as an acceptable rate capacity of 89 mAh g^{-1} at a high rate of 30 C. The excellent electrochemical performance of the $Li_4Ti_5O_{12}$-TiO_2 composite is attributed to the unique micro/nano and multiphases structure. The micro/nano structure enhances the structure stability and shortens the diffusion distance for both electron and lithium ions. Moreover, the abundant phase interfaces and grain boundaries store extra lithium ions and guarantee rapid lithium insertion/extraction kinetics.

Introduction

Green energy conversions and electrical energy storage systems, such as batteries

Corresponding author. Fax: +86 571 87953054. E-mail address: msewj01@zju.edu.cn (X. Z. Guo).

and supercapacitors, have attracted great attention to alleviate the increasingly severe challenges of global energy crisis and climate change. Rechargeable lithium-ion batteries (LIBs) have garnered particular interests due to large energy density, environmental friendliness and high safety, which are regarded as one of the most promising power sources for portable electronic devices and electrical/hybrid vehicles.[1-8] Nowadays, graphite-based materials have been widely used as commercial anode materials, which suffer the safety issues derived from the Li dendrites formed on carbon material surface when the potential approaches almost 0 V (vs. Li/Li^+) at the end of Li insertion and the capacity decay resulting from the formation of solid electrolyte interface (SEI) layer.[9,10] Hence, to meet the ever-increasing performance demands and to overcome safety issues, the search for alternative anode materials has become a consequential task in the LIBs field. Spinel lithium titanium ($Li_4Ti_5O_{12}$) has been considered as one of the promising alternative anode materials to graphite due to the almost near-zero structural changes (<1%) during repeated charge-discharge processes (ensuring good structure stability and high cycle reversibility) and a relatively high and flat operating voltage of 1.55 V (vs. Li/Li^+) for lithium storage (avoiding the formation of Li dendrites and the SEI layer), which delivers a theoretical capacity of 175 mAh g^{-1} with accommodating up to three additional Li^+ in its spinel structure. However, the practical application of $Li_4Ti_5O_{12}$ is still largely restrained by the low intrinsic electrical conductivity (10^{-13} S cm^{-1}) and the small lithium diffusion coefficient (10^{-13} to 10^{-9} cm^2 s^{-1}).[11-15]

Great efforts have been undertaken to overcome the obstacles of $Li_4Ti_5O_{12}$. The

design of micro/nano-structured materials has been demonstrated an effective strategy to improve the performance of $Li_4Ti_5O_{12}$. The micro/nano-structured materials possess the characteristics of microscale particles assembled or constructed from nanoscale components.[4,16-18] On the one hand, the micron-sized particles contribute to higher tap density, improved initial coulombic efficiency and volume specific capacity. On the other hand, large specific surface area and short pathways for Li^+ ions insertion/extraction can be provided by these nanoscale components. In addition, the porous structure derived from these micro/nano-structured materials has been proven to allow better penetration of the electrolyte, and accommodate the large volume changes during charging and discharging.[19-25] Recently, duplex phase $Li_4Ti_5O_{12}$-TiO_2 materials have been reported to show better electrochemical performance than pure $Li_4Ti_5O_{12}$ materials. It is believed that the improved electrochemical properties are attributed to the unique advantages of $Li_4Ti_5O_{12}$-TiO_2 composites: Firstly, Li insertion/extraction kinetics can be enhanced by the introduce of anatase TiO_2 and rutile TiO_2 ($\sim 10^{-6}$ cm^2 s^{-1}).[26-29] Secondly, the high theoretical capacity of anatase TiO_2 ($\sim$336 mAh g^{-1}) and the extra lithium storage of grain boundaries and phase interfaces make contribute to improving the reversible capacity of $Li_4Ti_5O_{12}$-TiO_2.[30-32] Moreover, the electronic transport and the surface charge transfer are accelerated by the high density of grain boundaries and phase interfaces.[11,33-35] As a result, the micro/nano structured $Li_4Ti_5O_{12}$-TiO_2 composites are anticipated to be promising anode materials for LIBs combine the merits of micro/nano structure and multiphase character.

Herein, we report the preparation of a porous ellipsoid-like $Li_4Ti_5O_{12}$-TiO_2 composite by a facile sol-gel route with subsequent heat treatment. Compared with solid-state reaction method reported in most studies[36-39], the strategy presented here shows low-temperature preparation and homogeneous distribution of chemical compositions. The as-prepared $Li_4Ti_5O_{12}$-TiO_2 composite presents a unique micro/nano structure comprised of numerous nanoscale crystals and multiphase constituent. Meanwhile, plenty of grain boundaries and phase interfaces are observed for the $Li_4Ti_5O_{12}$-TiO_2 composite. To the best of our knowledge, this is the first time to prepare ellipsoid-like $Li_4Ti_5O_{12}$-based materials with a unique micro/nano structure by sol-gel method. The electrochemical properties of the as-prepared $Li_4Ti_5O_{12}$-TiO_2 composite are investigated as an anode material for LIBs. Owing to the micro/nano porous structure and multiphase feature, the resultant $Li_4Ti_5O_{12}$-TiO_2 composite exhibits excellent high-rate performance and cycling stability.

Experimental section

Materials synthesis. Tetrabutyl titanate ($Ti(OC_4H_9)_4$, TBOT, Aladdin) and lithium acetate dihydrate ($CH_3COOLi•2H_2O$, LiAc, Sinopharm Chemical Reagent Co., Ltd (China)) were used as titanium and lithium sources, respectively. Mixtures of distilled water (H_2O) and ethanol (EtOH, 99.5%) were used as the solvents. Glacial acetic acid (HAc, Sinopharm Chemical Reagent Co., Ltd (China)) was used as catalyst for gelation. Poly(ethylene oxide) (PEO, Aladdin, M_w=300,000) was used as a phase separation inducer. All chemicals were of analytical grade and used as received.

The overall fabrication procedure is schematically illustrated in Fig. 1. In a typical synthesis, with the molar ratio of Li/Ti at 3.8:5, 15 mL TBOT (44 mM) and a certain amount of $LiAc{\cdot}2H_2O$ were dissolved in 25 mL EtOH to obtain solution A. 2.5 mL HAc, 3 mL deionized water and 20 mL EtOH were mixed, then 1.5 g PEO was added followed by stirring about 30 min to gain solution B. Then, the solution B was slowly dropped into the solution A with vigorous stirring at room temperature. After continuously stirring for 5 min, the mix solution was kept in a sealed container at 60 °C for gelation, and the white wet gels could be obtained after about 20 min. After dried in vacuum at 80 °C for 2 d, the resulting dried gels were heat-treated in a tube furnace at 600 °C for 5 h to obtain the final $Li_4Ti_5O_{12}$-TiO_2 composite. For comparison, the pure $Li_4Ti_5O_{12}$ was also prepared with stoichiometric amounts of TBOT (15 mL, 44 mM) and $LiAc{\cdot}2H_2O$.

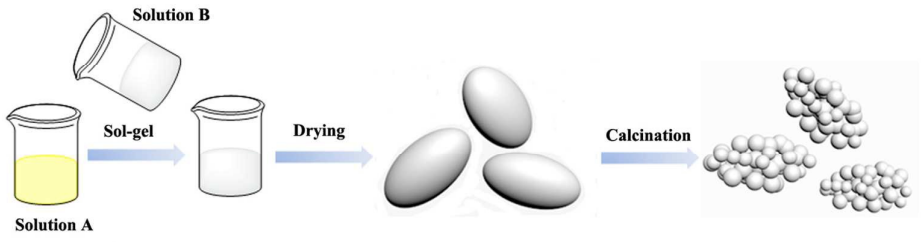

Fig. 1 Schematic representation of the fabrication procedure of micro/nano-structured ellipsoid-like $Li_4Ti_5O_{12}$-TiO_2 composite.

Structure characterizations. The composition of as-prepared products was studied by powder X-ray diffractometry (XRD; X'Pert Pro diffractometer with a Cu Kα radiation, λ =0.15418 nm). Morphology and microstructure were characterized using scanning electron microscopy (SEM; Hitachi S-4800) and transmission electron microscopy (TEM; FEI, Tecnai G2 F20). X-ray photoelectron spectroscopy (XPS) measurements were performed on a Thermo

ESCALAB 250 system to analyze the chemical valence state of elements using a monochromatic Al-Kα (1486.6 eV) as the X-ray source. The thermal decomposition behavior of the precursor was examined by thermogravimetric analysis (TGA, TA Q500) and differential thermal analysis (DTA, WRT-3P) at a heating rate of 10 °C min^{-1} from the room temperture to 800 °C in air. Nitrogen adsorption/desorption test was conducted by a nitrogen adsorption–desorption apparatus (AUTOSORB-1-C). Specific surface area and pore size distributions were calculated using the Brunauer-Emmett-Teller (BET) and Barrett-Joyner-Halenda (BJH), respectively.

Electrochemical measurements. Electrochemical experiments were performed using standard CR 2025 type coin cells in which a lithium metal foil was used as the counter and reference electrodes. Active material (as-prepared samples), carbon black (Super P) and polyvinylidene fluoride (PVDF) binder were mixed at a weight ratio of 80:10:10 in N-methyl-2-pyrrolidene (NMP) solution to form a slurry. The slurry was pasted on a Cu foil and dried in a vacuum oven at 120 ^{o}C for 12 h prior to coin-cell assembly. The loading density of the active materials in the electrode sheet was about 3 mg cm^{-2}. A solution of 1 M $LiPF_6$ in ethylene carbonate (EC)/dimethyl carbonate (DMC) (1:1 by volume) was employed as the electrolyte, and a polypropyle microporous film (Cellgard 2300) as the separator. Galvanostatic charge-discharge measurements were carried out on a Neware battery test system in the voltage range of 1.0-3.0 V. Cyclic voltammetry (CV) tests were performed between 1.0 and 3.0 V at a scan rate of 0.1 mV s^{-1} on a

CHI660b electrochemical workstation (Shanghai Chenhua, China). The electrochemical impedance spectroscopy (EIS) measurements were recorded on the same workstation with the frequency ranging from 0.1 Hz to 100 KHz with an amplitude of 5 mV.

Results and discussion

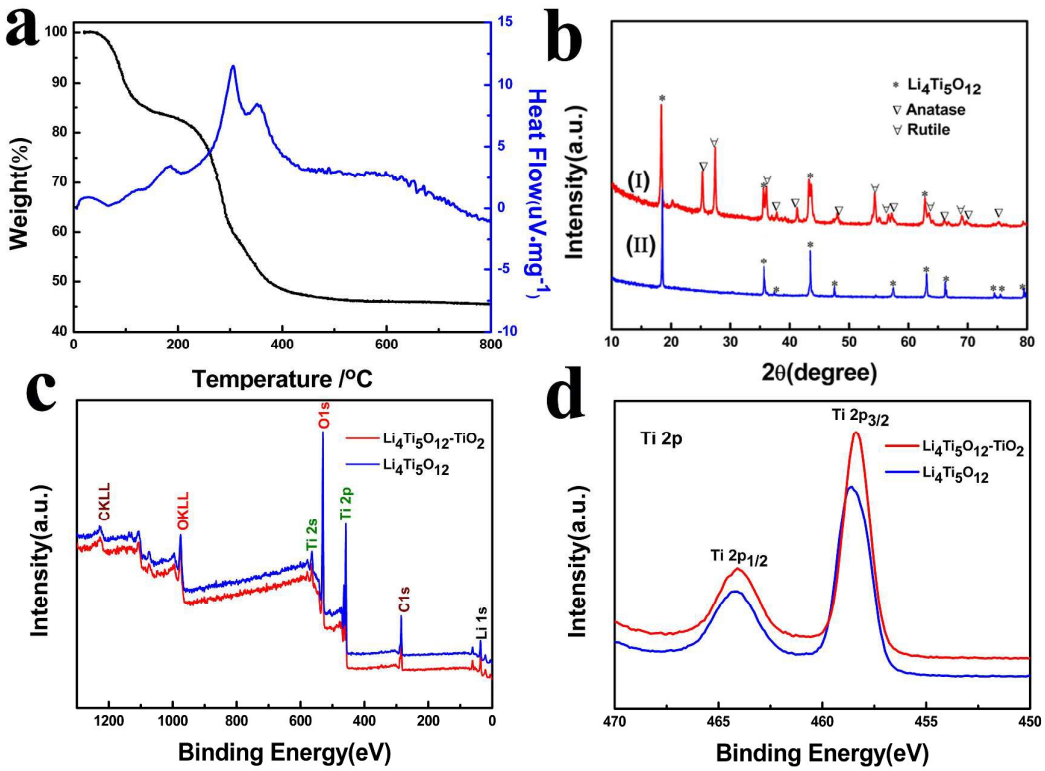

Fig. 2 (a) TG-DTA curve of the as-prepared dried gel with the Li/Ti molar ratio of 3.8:5. (b)XRD patterns of the heat-treated samples with different molar ratios between Li and Ti: (Ⅰ) Li/Ti = 3.8:5, (Ⅱ) Li/Ti = 4:5. XPS survey spectra spectrum (c) and high-resolution Ti 2p spectra (d) of pure $Li_4Ti_5O_{12}$ and $Li_4Ti_5O_{12}$-TiO_2 composite.

The thermogravimetry (TG)-differential thermal analysis (DTA) of the dried gel is shown in Fig. 2a. It can be found that there are two distinct weight loss in the temperature range of room temperature to 800 °C. The first weight loss of 15 % with a small endothermic peak up to 200 °C is primarily owing to the removal of absorbed/trapped water and organic solvent. Subsequently, a large weight loss of

about 37 % with several exothermic peaks can be detected between 200 and 500 °C, which is ascribed to the decomposition of PEO residue and the thermal reaction of precursor.[40,41] Finally, no obvious weight loss is observed above 500 °C, demonstrating the end of phase transformation and that any further heating only makes the structure of samples more crystallization. According to the TG-DTA results, the heat treatment temperature of 600 °C is chosen to calcinate the products in this work.

Fig. 2b shows the X-ray diffraction (XRD) patterns of as-obtained samples with different Li/Ti molar ratios after heat-treatment at 600 °C. The pure $Li_4Ti_5O_{12}$ phase can be obtained at the stoichiometric ratio of Li/Ti, all the diffraction peaks can be indexed to spinel $Li_4Ti_5O_{12}$ (JCPDS No. 49-0207).[42] The anatase and rutile of TiO_2 appear when the ratio (Li/Ti) decreases to 3.8:5, according to the PDF Cards (JCPDS No. 65-5714 and JCPDS No. 65-1119). The average crystallite sizes of $Li_4Ti_5O_{12}$ and $Li_4Ti_5O_{12}$-TiO_2 composite were determined by Scherrer equation using Jade software, which were calculated to be 46 and 48 nm, respectively. Moreover, high crystallinity of both two samples after the calcination at 600 °C is confirmed by the sharp XRD peaks in Fig. 2b, consistent with the TG-DTA curves in Fig. 2a.

X-ray photoelectron spectroscopy (XPS) measurements were carried out to further investigate the surface chemical compositions and elemental states of the as-prepared samples. The binding energies were corrected with reference to the C1s peak at 284.6 eV. As shown in Fig. 2c, obvious peaks of O1s, Ti2p, N1s, C1s

and Li1s peaks are observed in the XPS survey spectrum, demonstrating the existence of these elements. High resolution XPS spectrums for Ti2p are depicted in Fig. 2d to verify the electronic states of Ti atom. It can be seen that the Ti2p spectrums of both samples comprise two symmetrical peaks at around 464.2 and 458.4 eV, corresponding to the typical $Ti2p_{1/2}$ and $Ti2p_{3/2}$ of Ti^{4+}.[43,44] Furthermore, there are no peaks of Ti^{3+} or Ti^{2+} are detected. The results of XPS indicate that the valence state of Ti ions for both samples is +4, which is in accordance with XRD patterns. Based on the results of XRD and XPS, the relative weight fractions of $Li_4Ti_5O_{12}$, anatase, and rutile for the $Li_4Ti_5O_{12}$-TiO_2 composite are determined to be about 88.55 %, 3.45 %, and 8.00 %, respectively. The molar ratio of Li:Ti in the as-synthesized $Li_4Ti_5O_{12}$-TiO_2 composite is very close to that of the starting composition.

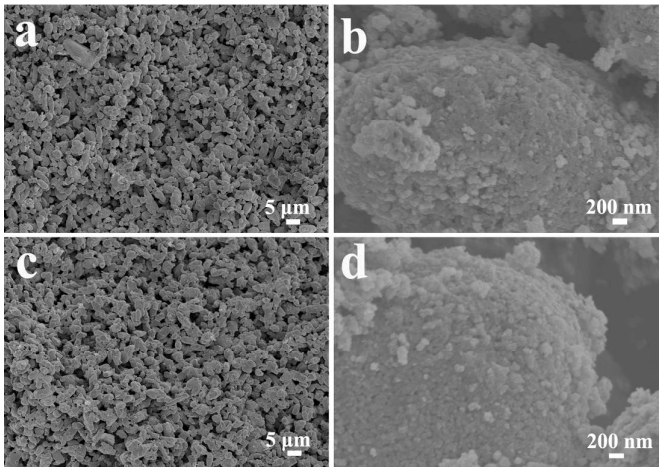

Fig. 3 Typical low and high-magnification SEM images of pure $Li_4Ti_5O_{12}$ (a,b) and $Li_4Ti_5O_{12}$-TiO_2 composite (c,d).

The morphologies of as-prepared products were characterized by scanning electron microscopy (SEM), as shown in Fig. 3. It is observed from the low-magnification SEM images (Fig. 3a and c) that both samples present an

ellipsoid-like morphology with a typical size in the range of 3-5 μm. These ellipsoid-like particles are formed due to the effect of phase-separation induced by PEO, which have been reported in our previous work.[40,45-47] The high-magnification SEM images (Fig. 3b and d) indicate that both of pure $Li_4Ti_5O_{12}$ and $Li_4Ti_5O_{12}$-TiO_2 composite display a coarse surface with an assembly of many fine nanocrystals due to the successive release and loss of CO_2 and H_2O during the thermal decomposition, which may be beneficial for high-rate capability and cycle stability by shortening the path of electron transport and lithium diffusion.

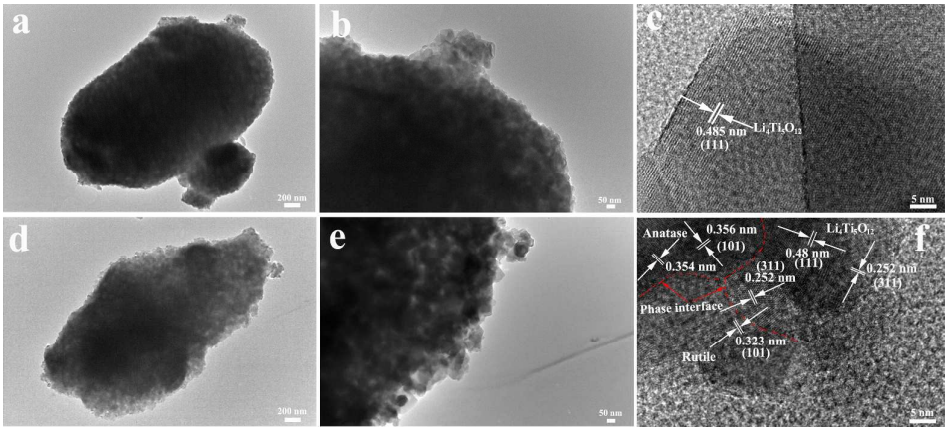

Fig. 4 TEM and HRTEM images of pure $Li_4Ti_5O_{12}$ (a-c) and $Li_4Ti_5O_{12}$-TiO_2 composite (d-f).

TEM and HRTEM characterizations were performed to further study the morphology and microstructure of pure $Li_4Ti_5O_{12}$ and $Li_4Ti_5O_{12}$-TiO_2 composite. As revealed in Fig. 4, both of samples display an ellipsoid-like particle morphology with microscale size (Fig. 4a and d) composed of numerous nanocrystals ranging from 30 to 80 nm (Fig. 4b and e), forming a porous structure, which agrees with XRD patterns and SEM observations. The lattice spacing of 0.485 nm in Fig. 4c corresponds to the (111) crystal plane of spinel $Li_4Ti_5O_{12}$.

Compared with pure $Li_4Ti_5O_{12}$, the distinct lattice stripes ascribed to the characteristic of TiO_2 can be detected from the $Li_4Ti_5O_{12}$-TiO_2 composite in Fig. 4f and Fig. S1. The measured fringe spacing values of spinel $Li_4Ti_5O_{12}$ are 0.48 and 0.252 nm, corresponding to (111) and (311) crystal planes of spinel $Li_4Ti_5O_{12}$, respectively. Moreover, the lattice spacing values of 0.356 and 0.323 nm are assigned to the (101) plane of anatase TiO_2 and rutile TiO_2, respectively, confirming the formation of $Li_4Ti_5O_{12}$-TiO_2 composite. Abundant grain boundaries and phase interfaces are produced due to nanocrystal components and different phases of $Li_4Ti_5O_{12}$ and TiO_2 (anatase and rutile), as marked by the red dashed line in Fig. 4f. The distinct lattice stripes in the HRTEM images (Fig. 4c and f) reveal that both of the pure $Li_4Ti_5O_{12}$ and $Li_4Ti_5O_{12}$-TiO_2 composite are well crystallized after the heat-treatment at 600 ^oC, which are consistent with the results of TG-DTA and XRD shown above.

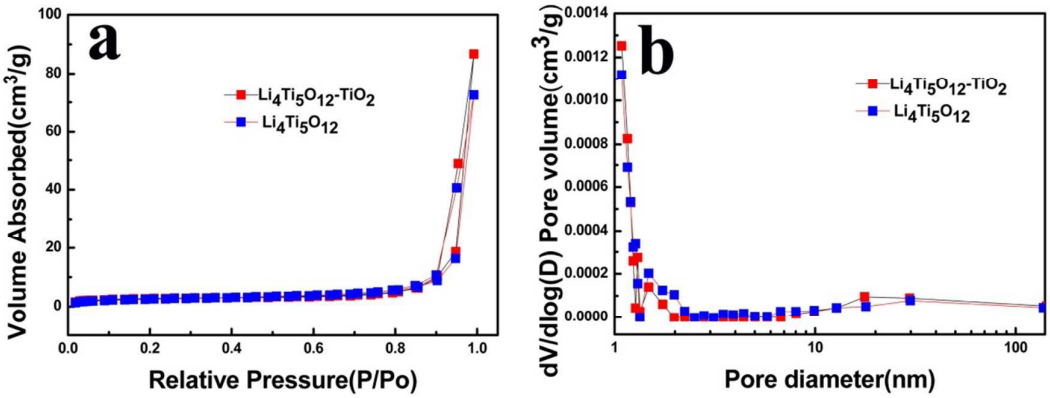

Fig. 5 Nitrogen adsorption-desorption isotherms (a) and pore size distributions curves (b) of pure $Li_4Ti_5O_{12}$ and $Li_4Ti_5O_{12}$-TiO_2 composite measured at 77 K.

N_2 adsorption/desorption measurements were conducted to further determine the pore structure of pure $Li_4Ti_5O_{12}$ and $Li_4Ti_5O_{12}$-TiO_2 composite. As presented in

Fig. 5, similar nitrogen adsorption–desorption isotherms and pore size distributions are observed for both samples, which display a typical type IV isotherms (Fig. 5a) with distinct hysteresis loops at high partial pressures according to the IUPAC classification, indicating the presence of mesopores and macropores possibly formed by the porous stacking of component nanoparticles.[48,49] Fig. 5b shows that the pore size is not uniform, and are calculated to be around 1.5 and 18.2 nm. Besides, the samples exhibit macropores with pore sizes of up to 100 nm, which could make contribute to providing good electrolyte access. The results are in good accordance with the SEM and TEM characterizations. The specific textural properties of the samples are shown as follows: the BET specific surface areas of pure $Li_4Ti_5O_{12}$ and $Li_4Ti_5O_{12}$-TiO_2 composite are 9.34 and 9.68 m^2 g^{-1}, respectively, and the corresponding pore volumes are 0.130 and 0.134 cm^3 g^{-1}, respectively.

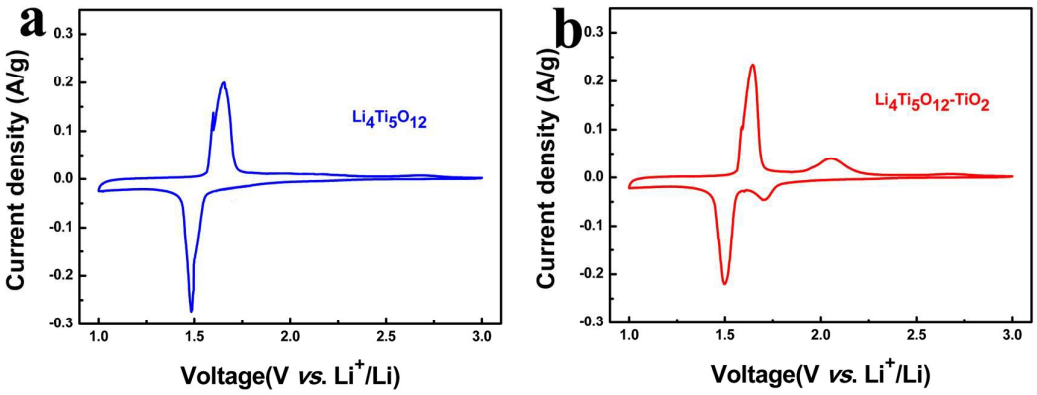

Fig. 6 CV curves of pure $Li_4Ti_5O_{12}$ (a) and $Li_4Ti_5O_{12}$-TiO_2 composite (b) electrodes at a scan rate of 0.1 mV s^{-1} in the potential window of 1.0-3.0 V.

Coin-cells were constructed to measure electrochemical performance of the fabricated pure $Li_4Ti_5O_{12}$ and $Li_4Ti_5O_{12}$-TiO_2 composite electrodes. Fig. 6 shows

the cyclic voltammogram (CV) curves of pure $Li_4Ti_5O_{12}$ and $Li_4Ti_5O_{12}$-TiO_2 composite at a scanning rate of 0.1 mV s^{-1} in the potential range of 1.0-3.0 V. As exhibited in Fig. 6a, the only one pair of oxidation/reduction peaks at around 1.65/1.48 V is observed for pure $Li_4Ti_5O_{12}$, corresponding to the redox reaction of Ti^{4+}/Ti^{3+} in spinel $Li_4Ti_5O_{12}$.[11,50] Compared with pure $Li_4Ti_5O_{12}$, an additional pair of redox peaks located at 1.70/2.05 V is detected for the $Li_4Ti_5O_{12}$-TiO_2 composite (Fig. 6b), which is attributed to the lithium insertion/extraction within the anatase TiO_2 lattices.[10,51-55]

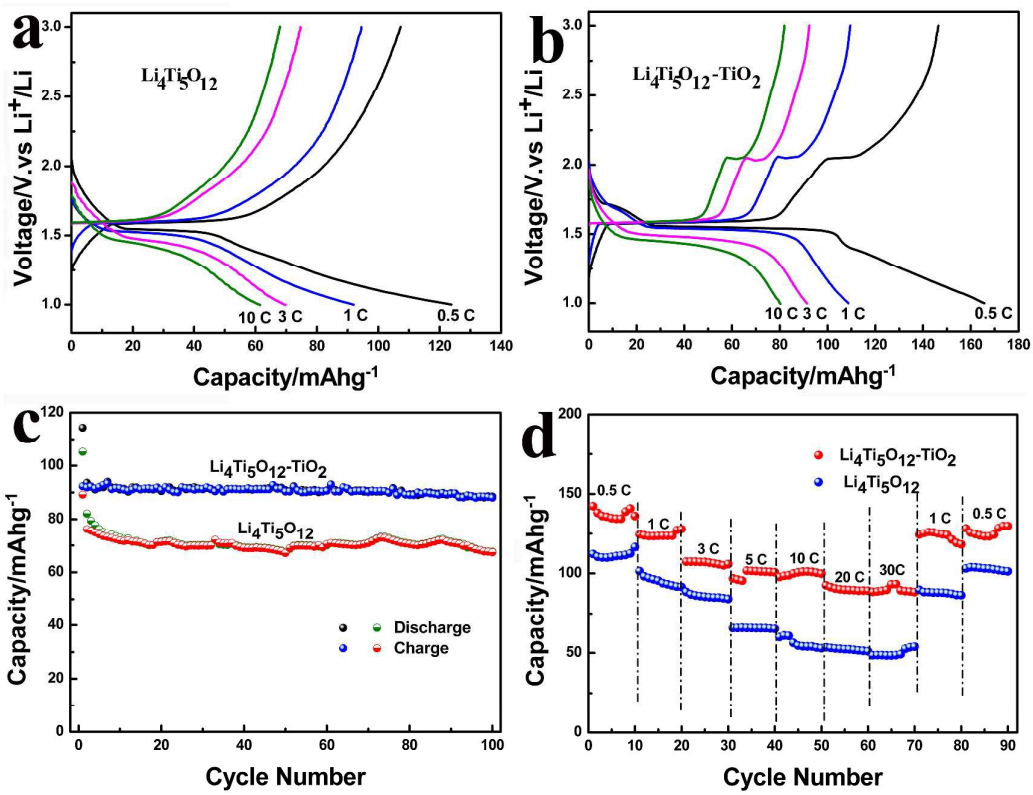

Fig. 7 Electrochemical properties of pure $Li_4Ti_5O_{12}$ and $Li_4Ti_5O_{12}$-TiO_2 composite: The initial galvanostatic charge-discharge curves profiles of (a) $Li_4Ti_5O_{12}$ and (b) $Li_4Ti_5O_{12}$-TiO_2 electrodes at different current densities from 0.5 to 10 C (1 C=175 mA g^{-1}), respectively. (c) Cycling performance at 10 C and (d) Rate performance at various current rates.

The electrochemical properties of pure $Li_4Ti_5O_{12}$ and $Li_4Ti_5O_{12}$-TiO_2 composite were evaluated and compared by galvanostatic charge-discharge tests.

The specific capacities are calculated based on the weight of the whole composites in this work. Fig. 7a and b show the initial galvanostatic charge/discharge profiles of pure $Li_4Ti_5O_{12}$ and $Li_4Ti_5O_{12}$-TiO_2 composite electrode at different current densities from 0.5 to 10 C (1 C= 175 mA g^{-1}) between 1.0 and 3.0 V vs Li^+/Li. Agree well with the result of CV curves (Figure 6), two long flat plateaus at about 1.51 and 1.62 V are observed in both $Li_4Ti_5O_{12}$ and $Li_4Ti_5O_{12}$-TiO_2 electrodes, which correspond to Li ions insertion/extraction in spinel $Li_4Ti_5O_{12}$ ($Li_4Ti_5O_{12}$+ $3Li^+$+ $3e^-$ ↔ $Li_7Ti_5O_{12}$). Moreover, at the rates of 0.5 C and 1 C, a short charge/discharge plateau at around 2.05 and 1.71 V is detected for the $Li_4Ti_5O_{12}$-TiO_2 composite, corresponding to the phase transformation from TiO_2 to Li_xTiO_2 ($xLi^+ + TiO_2 + xe^- \leftrightarrow Li_xTiO_2$). However, the discharge voltage plateaus of TiO_2 gradually disappear with the increase of C-rate, which is attributed to the polarization and unsaturated insertion/extrusion of Li^+ at high current densities. No plateau corresponding to the lithiation/delithiation process of rutile TiO_2 is detected for the $Li_4Ti_5O_{12}$-TiO_2 composite, indicating that the poor electrochemical activity for rutile TiO_2 in the sample.[26] Initial discharge capacities of pure $Li_4Ti_5O_{12}$ and $Li_4Ti_5O_{12}$-TiO_2 composite are measured to be 124 and 166 mAh g^{-1}, respectively. Some irreversible capacity loss is observed in the first cycle, which might be attributed to the irreversible electrochemical decomposition of electrolyte or impurity phase over the $Li_4Ti_5O_{12}$-TiO_2 surface.[33,35] It can be found that the discharge capacities of all samples decrease with increasing C-rate, the discharge capacities of $Li_4Ti_5O_{12}$-TiO_2 composite are calculated to be 108, 91 and 80 mAh

g^{-1} at 1, 3, and 10 C rates, respectively. And the values for pure $Li_4Ti_5O_{12}$ are 92, 70 and 62 mAh g^{-1} at the same rates. The improved capacity of $Li_4Ti_5O_{12}$-TiO_2 composite in comparison with pure $Li_4Ti_5O_{12}$ is contributed by the high specific capacity of TiO_2 and the extra lithium storage derived from phase interfaces.

Fig. 7c compares the cycling performance of pure $Li_4Ti_5O_{12}$ at 10 C with that of $Li_4Ti_5O_{12}$-TiO_2 composite in the voltage range of 1.0-3.0 V. It can be found that the $Li_4Ti_5O_{12}$-TiO_2 composite electrode delivers a higher capacity and better cycling performance. The reversible capacity of $Li_4Ti_5O_{12}$-TiO_2 composite is 92 mAh g^{-1} after 100 cycles, which is about 96% of the initial capacity, exhibiting an excellent cycle stability. On the contrary, the reversible capacity of pure $Li_4Ti_5O_{12}$ decreases quickly upon cycles due to the large polarization of electrodes, only 67 mAh g^{-1} could be maintained after 100 cycles. The $Li_4Ti_5O_{12}$-TiO_2 composite presents a relative lower capacity in comparison with the work reported by Yin et al[56] and some examples given in the review by Yi et al[57], which may attributed to the relatively small specific surface area (Fig. 5) derived from the large-size particles and inter-particle aggregation.[58,59] Moreover, like some reported works, the low capacity may due to the existence of rutile TiO_2 (about 8.00 %), which delivers a capacity of ≈50 mAh g^{-1} with insert/extract of negligible amounts of Li^+.[60,61] Ongoing work shows the capacity of the ellipsoid-like $Li_4Ti_5O_{12}$-TiO_2 composite can be improved by optimizing the experimental process. However, the $Li_4Ti_5O_{12}$-TiO_2 composite shows a superior cycle stability with negligible capacity decay after 100 cycles. It is reasonable to assume that the improved cycling

stability for the $Li_4Ti_5O_{12}$-TiO_2 composite is related to the modification of TiO_2.[62]

The rate performance of pure $Li_4Ti_5O_{12}$ and $Li_4Ti_5O_{12}$-TiO_2 composite were studied by progressively charging/discharging from 0.5 to 30 C for 10 cycles at each rate, and then again at 1 and 0.5 C for 10 cycles, as shown in Fig. 7d. The result is in good accordance with Fig. 7c, the $Li_4Ti_5O_{12}$-TiO_2 composite exhibits superior rate capability in comparison with pure $Li_4Ti_5O_{12}$. It can be observed that the rate capacities of both samples decrease regularly with the increase of current densities. Compared with pure $Li_4Ti_5O_{12}$, much higher discharge capacities can be delivered for the $Li_4Ti_5O_{12}$-TiO_2 composite at the same rates, especially at high rate. A high capacity of 89 mAh g^{-1} can be achieved for the $Li_4Ti_5O_{12}$-TiO_2 composite at the rate as high as 30 C, whereas the value drops to only 46 mAh g^{-1} for pure $Li_4Ti_5O_{12}$ at the same rate. The significantly improved rate capability of the $Li_4Ti_5O_{12}$-TiO_2 composite compared to that of pure $Li_4Ti_5O_{12}$ is attributed to the synergistic effect of the superior theoretical capacity of anatase TiO_2 materials, high lithium diffusion rate derived from rutile TiO_2 and extra lithium storage contibuted by grain boundary and phase interface. The result is consistent with the previous work reported by Chen *et. al*[11] and Yi *et. al*[62]. Moreover, when the current density is returned to 1 and 0.5 C again, specific capacities of both samples can be recovered to a large extent due to the unique micro/nano porous structure, and keep stable during continuous discharge/charge cycles.

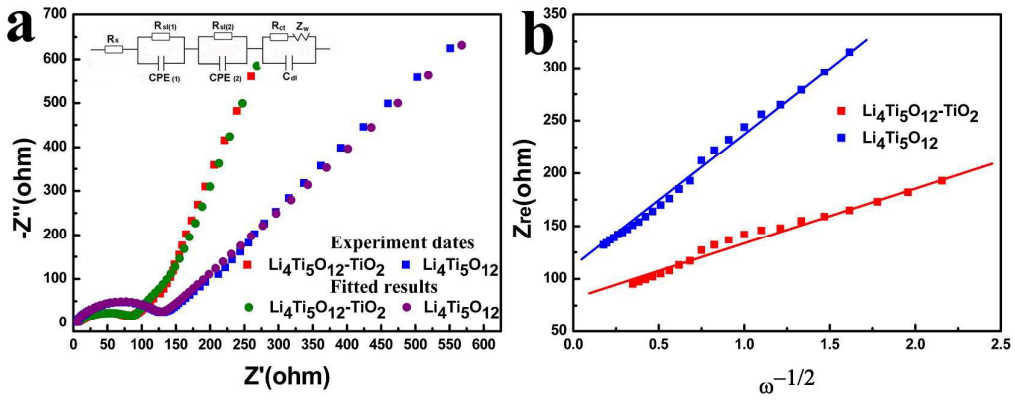

Fig. 8 (a) Electrochemical impedance spectra (Nyquist plots) and corresponding simulation results of pure $Li_4Ti_5O_{12}$ and $Li_4Ti_5O_{12}$-TiO_2 composite. The inset is the equivalent circuit used for plots fitting. (b) Graph of Z_{re} plotted against $\omega^{-1/2}$ at low frequency region of pure $Li_4Ti_5O_{12}$ and $Li_4Ti_5O_{12}$-TiO_2 composite.

Electrochemical impedance spectroscopy (EIS) measurements were performed to investigate the enhanced rate capability of $Li_4Ti_5O_{12}$-TiO_2 composite electrode. Nyquist plots of pure $Li_4Ti_5O_{12}$ and $Li_4Ti_5O_{12}$-TiO_2 composite electrodes are depicted in Fig. 8a. Typically, both the Nyquist plots consist of a depressed semicircle in the high-middle frequency regions and a slopping straight line in the low frequency region. The diameter of the semicircle is mainly related to the surface charge transfer resistance (Rct), associated with the interfacial electrochemical reaction activity, and the sloping straight line in low frequency region corresponds to the lithium ion diffusion process in the electrodes. Nyquist plots are fitted using the equivalent circuit (inset of Fig. 8a). In this equivalent circuit, R_s represents the solution resistance, R_{sl} (i) and CPE (i) (i = 1, 2) correspond to the migration of hydrogen ions and the capacity of the layer, respectively[63]. R_{ct} and C_{dl} reflect the charge-transfer resistance and a double-layer capacitance, respectively.[2] Z_W is the Warburg impedance. Obviously, the $Li_4Ti_5O_{12}$-TiO_2 composite presents a smaller circle compared with pure $Li_4Ti_5O_{12}$,

which indicates that the $Li_4Ti_5O_{12}$-TiO_2 composite (Rct =88 Ω) possesses a lower charge transfer resistance than that of pure $Li_4Ti_5O_{12}$ (Rct =130 Ω). The result indicates that the electrical conductivity of $Li_4Ti_5O_{12}$-TiO_2 composite is greatly increased compared with pure $Li_4Ti_5O_{12}$, which is favorable for the improvement of rate performance. Meanwhile, the different slopes in the low frequency can be detected for pure $Li_4Ti_5O_{12}$ and $Li_4Ti_5O_{12}$-TiO_2 composite, implying the different lithium ion diffusion rate for both samples. The diffusion coefficient (D_{Li}) of lithium ion can be calculated from the plots in the low-frequency region according to the following equations[64,65]:

$$D=R^2T^2/2A^2n^4F^4C_{Li}^2\sigma^2 \quad (1)$$

$$Z_{re}=R_e+R_{ct}+\sigma\omega^{-1/2} \quad (2)$$

Where R is the gas constant, T the absolute temperature, A the surface area of the electrode, n the number of electrons transferred in the half-reaction for the redox couple, F the Faraday constant, C_{Li} the concentration of lithium ion in solid, and σ is the Warburg factor, which is relative to Z_{re}-σ and can be obtained from the slope of the lines in Fig. 8b. As expressed in above equations, it is clear that D is inversely proportional to σ. Furthermore, the slope of the linear fitting lines of Z_{re} *vs*. ω is σ. As shown in Fig. 8b, the $Li_4Ti_5O_{12}$-TiO_2 composite has a smaller slope compared to pure $Li_4Ti_5O_{12}$, demonstrating that it has a higher Li^+ diffusion coefficient. These results imply that the $Li_4Ti_5O_{12}$-TiO_2 composite has higher charge transfer kinetics and ionic mobility than pure $Li_4Ti_5O_{12}$, which could ascribed to the contribution of anatase TiO_2, rutile TiO_2, and abundant phase

interfaces and grain boundaries. The results of EIS could well explain the better electrochemical performance of the $Li_4Ti_5O_{12}$-TiO_2 composite shown in Fig. 7.

The $Li_4Ti_5O_{12}$-TiO_2 composite reported here presents excellent rate capability and cycling stability, which are compared favourably to other dual phase $Li_4Ti_5O_{12}$-TiO_2 based electrodes reported in the literatures.[33,44,66,67] The superior electrochemical performance of the ellipsoid-like $Li_4Ti_5O_{12}$-TiO_2 composite is attributed to the synergistic effects of unique micro/nano porous structure and large number of grain boundaries and phase interfaces. Firstly, micro/nano $Li_4Ti_5O_{12}$-TiO_2 composite constructed from nanocrystallines, which facilitate the permeation of electrolyte within the electrode and shorten the diffusion distance for both electron and lithium ions. Secondly, the higher theoretical capacity of anatase TiO_2 could contributes partial capacity to the improved capacity of the $Li_4Ti_5O_{12}$-TiO_2 composite. Furthermore, overall conductivity of the electrode and the transportation of lithium ions can be enhanced by the existence of anatase TiO_2 and rutile TiO_2 in the $Li_4Ti_5O_{12}$-TiO_2 composite, resulting in excellent high rate capability. Thirdly, the pseudocapacitive and extra lithium ions storage derived from grain boundaries and phase interfaces in the $Li_4Ti_5O_{12}$-TiO_2 composite make contribution to increasing the specific capacity. Moverover, the abundant phase interfaces can also improve the kinetics of the electrode, ensuring the fast lithium ion insertion/extraction reaction. In additon, the porous structure could effectively accommodate the stress induced during the charge/discharge process, which results in good structural and cycling stability.

Conclusion

In summary, porous ellipsoid-like $Li_4Ti_5O_{12}$-TiO_2 composite composed of nanocrystals has been fabricated through a facile sol-gel process and subsequent calcination treatment. The structure and electrochemical performance of pure $Li_4Ti_5O_{12}$ and $Li_4Ti_5O_{12}$-TiO_2 composite have been investigated in detail. Compared with pure $Li_4Ti_5O_{12}$, the $Li_4Ti_5O_{12}$-TiO_2 composite exhibits superior cycling performance and rate capability, which could attributed to the synergistic effect of the unique porous micro/nano structure, abundant phase interfaces, and grain boundaries. The remarkable electrochemical performance suggests that this ellipsoid-like $Li_4Ti_5O_{12}$-TiO_2 composite with micro/nano porous structure could be a promising anode material for advanced lithium ion batteries, and we believe that this facile strategy can be extensively applied to synthesize other micro/nano structured materials.

Acknowledgements

This work was supported by the National Natural Science Foundation of China (51372225), and the Natural Science Foundation of Zhejiang Province, China (LY13B010001).

Notes and references

1 M. M. Rahman, J. Z. Wang, M. F. Hassan, D. Wexler and H. K. Liu, *Adv Energy Mater*, 2011, **1**, 212.

2 Y. Xia, Z. Xiao, X. Dou, H. Huang, X. H. Lu, R. J. Yan, Y. P. Gan, W. J. Zhu, J. P. Tu, W. K. Zhang and X. Y. Tao, *Acs Nano*, 2013, **7**, 7083.

3 H. Huang, W. Zhu, X. Tao, Y. Xia, Z. Yu, J. Fang, Y. Gan and W. Zhang, *Acs Appl Mater Inter*, 2012, **4**, 5974.

4 P. J. Zhang, L. B. Wang, J. Xie, L. W. Su and C. A. Ma, *J Mater Chem A*, 2014, **2**, 3776.

5 W. Zhu, H. Huang, Y. Gan, X. Tao, Y. Xia and W. Zhang, *Electrochim Acta*, 2014, **138**, 376.

6 W. Zhu, H. Huang, W. Zhang, X. Tao, Y. Gan, Y. Xia, H. Yang and X. Guo, *Electrochim Acta*, 2015, **152**, 286.

7 H. Xiao, Y. Xia, W. K. Zhang, H. Huang, Y. P. Gan and X. Y. Tao, *J Mater Chem A*, 2013, **1**, 2307.

8 S. H. Liu, H. P. Jia, L. Han, J. L. Wang, P. F. Gao, D. D. Xu, J. Yang and S. N. Che, *Adv Mater*, 2012, **24**, 3201.

9 G. D. Du, N. Sharma, V. K. Peterson, J. A. Kimpton, D. Z. Jia and Z. P. Guo, *Adv Funct Mater*, 2011, **21**, 3990.

10 W. Zhu, H. Yang, K. Nakanishi, K. Kanamori and X. Guo, *Rsc Adv*, 2015, **5**, 24803.

11 J. Y. Liao, V. Chabot, M. Gu, C. M. Wang, X. C. Xiao and Z. W. Chen, *Nano Energy*, 2014, **9**, 383.

12 L. Yu, H. B. Wu and X. W. Lou, *Adv Mater*, 2013, **25**, 2296.

13 L. Sun, J. P. Wang, K. L. Jiang and S. S. Fan, *J Power Sources*, 2014, **248**, 265.

14 Y. Sun, L. Zhao, H. Pan, X. Lu, L. Gu, Y.-S. Hu, H. Li, M. Armand, Y. Ikuhara and L. Chen, *Nat Commun*, 2013, **4**, 1870.

15 D. Kim, Y. Ahn and J. Kim, *Electrochem Commun*, 2005, **7**, 1340.

16 G. Y. Huang, S. M. Xu, Z. H. Xu, H. Y. Sun and L. Y. Li, *Acs Appl Mater Inter*, 2014, **6**, 21325.

17 B. Zhang, Y. B. Zhang, Z. Z. Miao, T. X. Wu, Z. D. Zhang and X. G. Yang, *J Power Sources*,

2014, **248**, 289.

18 Y. F. Tang, L. Yang, Z. Qiu and J. S. Huang, *J Mater Chem*, 2009, **19**, 5980.

19 Z.-J. Han, N. Yabuuchi, K. Shimomura, M. Murase, H. Yui and S. Komaba, *Energ Environ Sci*, 2012, **5**, 9014.

20 G. Huang, S. Xu, S. Lu, L. Li and H. Sun, *Electrochim Acta*, 2014, **135**, 420.

21 L. Wang, B. Liu, S. Ran, L. Wang, L. Gao, F. Qu, D. Chen and G. Shen, *J Mater Chem A*, 2013, **1**, 2139.

22 Y. S. Lin, J. G. Duh, M. C. Tsai and C. Y. Lee, *Electrochim Acta*, 2012, **83**, 47.

23 J. Z. Chen, L. Yang, S. H. Fang, S. Hirano and K. Tachibana, *J Power Sources*, 2012, **200**, 59.

24 J. S. Chen, L. A. Archer and X. W. Lou, *J Mater Chem*, 2011, **21**, 9912.

25.M. Osiak, H. Geaney, E. Armstrong and C. O'Dwyer, *J Mater Chem A*, 2014, **2**, 9433.

26 J. S. Chen and X. W. Lou, *J Power Sources*, 2010, **195**, 2905.

27 J. S. Chen and X. W. Lou, *Electrochem Commun*, 2009, **11**, 2332.

28 Y. Yang, X. Ji, M. Jing, H. Hou, Y. Zhu, L. Fang, X. Yang, Q. Chen and C. E. Banks, *J Mater Chem A*, 2015, **3**, 5648.

29 W. Zhu, H. Yang, Y. Xie, S. Sun and X. Guo, *Mater Res Bull*, 2015,**73**,48.

30 H. B. Wu, X. W. Lou and H. H. Hng, *Chem-Eur J*, 2012, **18**, 3132.

31 S. J. Ding, J. S. Chen, D. Y. Luan, F. Y. C. Boey, S. Madhavi and X. W. Lou, *Chem Commun*, 2011, **47**, 5780.

32 L. Gao, S. Li, D. Huang, Y. Shen and M. Wang, *J Mater Chem A*, 2015, **3**, 10107.

33 M. Rahman, J. Z. Wang, M. F. Hassan, D. Wexler and H. K. Liu, *Adv Energy Mater*, 2011, **1**, 212.

34 J. Wang, H. L. Zhao, Q. Yang, C. M. Wang, P. P. Lv and Q. Xia, *J Power Sources*, 2013, **222**, 196.

35 F. Wu, X. Li, Z. Wang and H. Guo, *Nanoscale*, 2013, **5**, 6936.

36 L. F. Shen, X. G. Zhang, E. Uchaker, C. Z. Yuan and G. Z. Cao, *Adv Energy Mater*, 2012, **2**, 691.

37 X. L. Yao, S. Xie, H. Q. Nian and C. H. Chen, *J Alloy Compd*, 2008, **465**, 375.

38 L. Wang, Q. Z. Xiao, Z. H. Li, G. T. Lei, P. Zhang and L. J. Wu, *J Solid State Electr*, 2012, **16**, 3307.

39 K. Zaghib, M. Simoneau, M. Armand and M. Gauthier, *J Power Sources*, 1999, **81**, 300.

40 X. Z. Guo, X. B. Cai, J. Song, Y. Zhu, K. Nakanishi, K. Kanamori and H. Yang, *New J Chem*, 2014, **38**, 5832.

41 C. Q. Du, Z. Y. Tang, J. W. Wu, H. Q. Tang and X. H. Zhang, *Electrochim Acta*, 2014, **125**, 58.

42 Y. Q. Wang, L. Guo, Y. G. Guo, H. Li, X. Q. He, S. Tsukimoto, Y. Ikuhara and L. J. Wan, *J Am Chem Soc*, 2012, **134**, 7874.

43 Y. Qiao, X. L. Hu, Y. Liu, C. J. Chen, H. H. Xu, D. F. Hou, P. Hu and Y. H. Huang, *J Mater Chem A*, 2013, **1**, 10375.

44 J. M. Sun, D. H. Teng, Y. Liu, C. Chi, Y. H. Yu, J. L. Lan and X. P. Yang, *Rsc Adv*, 2014, **4**, 48632.

45 W. Y. Li, Y. Zhu, X. Z. Guo, K. Nakanishi, K. Kanamori and H. Yang, *Sci Technol Adv Mat*, 2013, **14**.

46 X. Z. Guo, W. Y. Li, K. Nakanishi, K. Kanamori, Y. Zhu and H. Yang, *J Eur Ceram Soc*, 2013, **33**, 1967.

47 X. Guo, W. Zhu, X. Cai, S. Liu and H. Yang, *Materials & Design*, 2015, **83**, 314.

48 Y. Tang, L. Yang, S. Fang and Z. Qiu, *Electrochim Acta*, 2009, **54**, 6244.

49 J. Liu, X. F. Li, J. L. Yang, D. S. Geng, Y. L. Li, D. N. Wang, R. Y. Li, X. L. Sun, M. Cai and M. W. Verbrugge, *Electrochim Acta*, 2012, **63**, 100.

50 J. Haetge, P. Hartmann, K. Brezesinski, J. Janek and T. Brezesinski, *Chem Mater*, 2011, **23**, 4384 .

51 Y. M. Jiang, K. X. Wang, X. Y. Wu, H. J. Zhang, B. M. Bartlett and J. S. Chen, *Acs Appl Mater Inter*, 2014, **6**, 19791.

52 B. C. Qiu, M. Y. Xing and J. L. Zhang, *J Am Chem Soc*, 2014, **136**, 5852.

53 H. Ren, R. B. Yu, J. Y. Wang, Q. Jin, M. Yang, D. Mao, D. Kisailus, H. J. Zhao and D. Wang, *Nano Lett*, 2014, **14**, 6679.

54 Y. Tang, Y. Zhang, J. Deng, D. Qi, W. R. Leow, J. Wei, S. Yin, Z. Dong, R. Yazami and Z. Chen, *Angewandte Chemie*, 2014, **126**, 13706.

55 W. Zhu, H. Yang, W. Zhang, H. Huang, X. Tao, Y. Xia, Y. Gan and X. Guo, *Rsc Adv*, 2015, **5**, 74774.

56 S. Y. Yin, L. Song, X. Y. Wang, M. F. Zhang, K. L. Zhang and Y. X. Zhang, *Electrochim Acta*, 2009, **54**, 5629.

57 T. F. Yi, L. J. Jiang, J. Shu, C. B. Yue, R. S. Zhu and H. B. Qiao, *J Phys Chem Solids*, 2010, **71**, 1236.

58 J. W. Zhang, F. L. Zhang, J. H. Li, W. Cai, J. W. Zhang, L. G. Yu, Z. S. Jin and Z. J. Zhang, *J Nanopart Res*, 2013, **15**.

59 Y. G. Wang, H. Q. Li, P. He, E. Hosono and H. S. Zhou, *Nanoscale*, 2010, **2**, 1294.

60 Y. S. Hu, L. Kienle, Y. G. Guo and J. Maier, *Adv Mater*, 2006, **18**, 1421.

61 S. W. Han, J. Jeong and D. H. Yoon, *Appl Phys a-Mater*, 2014, **114**, 925.

62 T. F. Yi, Z. K. Fang, Y. Xie, Y. R. Zhu and S. Y. Yang, *Acs Appl Mater Inter*, 2014, **6**, 20205.

63 G. F. Cai, J. P. Tu, D. Zhou, J. H. Zhang, Q. Q. Xiong, X. Y. Zhao, X. L. Wang and C. D. Guts, *J Phys Chem C*, 2013, **117**, 15967.

64 S.-L. Chou, J.-Z. Wang, H.-K. Liu and S.-X. Dou, *The Journal of Physical Chemistry C*, 2011, **115**, 16220.

65 J. Chen, L. Yang, S. Fang, S.-i. Hirano and K. Tachibana, *J Power Sources*, 2012, **200**, 59.

66.J. Y. Liao, X. C. Xiao, D. Higgins, D. G. Lee, F. Hassan and Z. W. Chen, *Electrochim Acta*, 2013, **108**, 104.

67 M. Armand and J.-M. Tarascon, *Nature*, 2008, **451**, 652.